ADVANCED MATERIALS
www.advmat.de

A Liquid Metal Microdroplets Initialized Hemicellulose Composite for 3D Printing Anode Host in Zn-Ion Battery

Ge Shi, Xinwen Peng, Jiaming Zeng, Linxin Zhong,* Yuan Sun, Wu Yang, Yu Lin Zhong, Yuxuan Zhu, Ren Zou, Shimelis Admassie, Zhaoqing Liu, Chuanfu Liu, Emmanuel I. Iwuoha, and Jun Lu**

Maintaining a steady affinity between gallium-based liquid metals (LM) and polymer binders, particularly under continuous mechanical deformation, such as extrusion-based 3D printing or plating/stripping of Zinc ion (Zn^{2+}), is very challenging. Here, an LM-initialized polyacrylamide-hemicellulose/EGaIn microdroplets hydrogel is used as a multifunctional ink to 3D-print self-standing scaffolds and anode hosts for Zn-ion batteries. The LM microdroplets initiate acrylamide polymerization without additional initiators and cross-linkers, forming a double-covalent hydrogen-bonded network. The hydrogel acts as a framework for stress dissipation, enabling recovery from structural damage due to the cyclic plating/stripping of Zn^{2+}. The LM-microdroplet-initialized polymerization with hemicelluloses can facilitate the production of 3D printable inks for energy storage devices.

1. Introduction

Strong and stable interactions between electrode materials are critical for the development of electrochemical storage devices. Conventional conductive inks consist of inorganic electrode materials and polymer binders.[1] The conventional conductive-ink electrodes undergo weak interactions due to mainly hydrogen bonding between the two components, exhibiting low operational stability. The weak interactions cause electrode degradation by active-material pulverization and electrode-material peel-off, reducing the active-material efficiency.[2] Additionally, conventional conductive-ink electrodes exhibit a limited surface area and restricted electrolyte immersion.[3]

Novel electrode materials with unique structures have been used to minimize the intrinsic degradation effects.[4] Gallium (Ga)-based liquid metal (LM), with excellent deformability, high conductivity, nontoxicity, and high chemical stability in air and aqueous environments,[5] exhibits immense potential as an electrode material for aqueous Zn-ion batteries.[6,7] However, using bulk LM as an electrode material is associated with two major drawbacks. First, due to the high density and liquidity of LM, the bulk LM electrode flows through the separator in the absence of a suitable polymer binder, causing a battery short-circuit.[8] Second, the plating/stripping of Zn^{2+} ions causes an LM-droplet loss from the electrode.[6]

A common strategy to overcome these limitations involves the incorporation of LM droplets into an ion-conductive polymer hydrogel.[6] However, simply mixing LM droplets within a polymer hydrogel generates insufficient interfacial bonding due to weak van der Waals interactions between the LM droplets and polymer chains. An LM-droplet organic-solvent treatment enables the synthesis of polymer composites with LM droplets; however, this strategy is unsuitable for batteries with aqueous electrolytes.[9] To address these limitations, it was hypothesized that using LM droplets as a monomer-polymerization initiator, instead of other widely-used ions,[10] could cross-link the polymer chains to form a 3D porous network with high stability under mechanical deformation.

In this study, bulk eutectic gallium-indium (EGaIn), consisting of 75 wt.% gallium and 25 wt.% indium, was converted to microdroplets through shear mixing to initiate the polymerization

G. Shi, X. Peng, J. Zeng, L. Zhong, Y. Sun, W. Yang, R. Zou, S. Admassie, C. Liu
State Key Laboratory of Pulp and Paper Engineering
South China University of Technology
Guangzhou, Guangdong 510640, China
E-mail: fexwpeng@scut.edu.cn; lxzhong0611@scut.edu.cn
Y. L. Zhong, Y. Zhu
Queensland Micro- and Nanotechnology Centre
School of Environment and Science
Griffith University
Nathan, QLD 4111, Australia
S. Admassie
Department of Chemistry
Addis Ababa Univeristy
PO BOX 1176, Addis Ababa Ethiopia
Z. Liu
School of Chemistry and Chemical Engineering/Institute of Clean Energy and Materials/Guangzhou Key Laboratory for Clean Energy and Materials/Huangpu Hydrogen Innovation Center
Higher Education Mega Center No. 230 Wai Huan Xi Road, Guangzhou 510006, China
E. I. Iwuoha
Department of Chemistry
University of the Western Cape (UWC)
Robert Sobukwe Road, Bellville, Cape Town 7535, South Africa
J. Lu
College of Chemical and Biological Engineering
Zhejiang University
Hangzhou, Zhejiang Province 310027, China
E-mail: junzoelu@zju.edu.cn

The ORCID identification number(s) for the author(s) of this article can be found under https://doi.org/10.1002/adma.202300109

DOI: 10.1002/adma.202300109

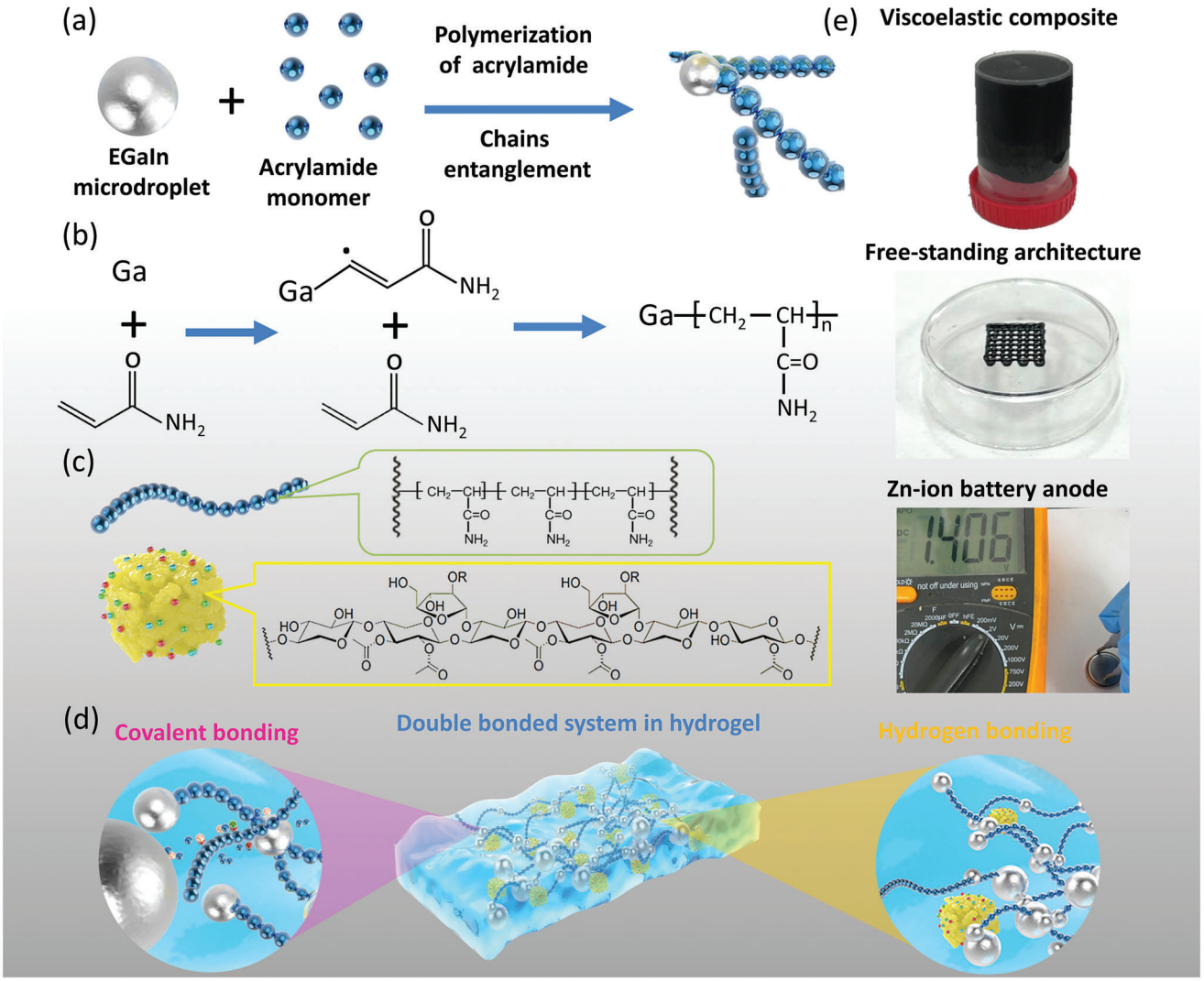

Figure 1. Schematic of the LM-initialized in situ polymerization of acrylamide with hemicellulose microparticles and using the resultant hydrogel as an ink to 3D print a scaffold and anode. a) The EGaIn LM microdroplets initiate radical polymerization between the microdroplets and acrylamide monomers. b) An unpaired electron from the microdroplets reacts with the π-bond of the vinyl monomer. c) Schematic illustration of the formation of hydrogen bonding between the polyacrylamide chain and the hemicellulose microparticle. d) Schematic of the hydrogel containing covalent bonds and hydrogen bonds. e) Digital photos of the viscoelastic composite, 3D printed polyacrylamide-hemicellulose/EGaIn microdroplets hydrogel scaffold and a Zn-ion battery using the composite as anode host.

of acrylamide monomers. The fabricated composite hydrogel was labeled as polyacrylamide-hemicellulose/EGaIn microdroplets hydrogel and used to 3D-print free-standing scaffolds and produce self-healable anode hosts for Zn-ion batteries.

The LM-initialized hydrogel was confirmed to be a double-covalent hydrogen-bonding system with self-healing and shear-thinning behavior that facilitated extrusion-based 3D printing. It contained homogeneously distributed LM microdroplets within a hemicellulose composite network that prevented battery short-circuits caused by LM droplet loss. Furthermore, the hydrogel acted as an electrically and ionically conductive microporous matrix for the isotropic deposition of Zn-ions to form a steady anode host capable of withstanding microstructural changes during the recyclable plating/stripping of Zn-ions.

2. Results and Discussion

2.1. LM-Initiated Acrylamide Polymerization

The formulation and free-radical polymerization of the LM-initialized polyacrylamide hydrogel (labeled polyacrylamide-hemicellulose/EGaIn microdroplets hydrogel) are shown in **Figure 1**a and Figure S1 (Supporting Information). The unpaired electrons of the Ga atoms on the surface of the EGaIn microdroplets facilitated acrylamide polymerization, while the hemicellulose microparticles acted as stabilizers to maintain the suspension of EGaIn microdroplets during the reaction. The free-radical polymerization of acrylamide and the influence of the hemicellulose microparticles have been discussed in this section.

The shear mixing of EGaIn LM in an aqueous solution of acrylamide and hemicellulose (Figure S1a–d, Supporting Information) was used for the free-radical polymerization of acrylamide. Shear mixing facilitates homogenized polymerization in large volumes (≥30 mL), as described in (Section 2 of the Supporting Information). Here, it separated bulk LM droplets into numerous microdroplets (Figure S1c,d, Supporting Information) which generated free radicals with unpaired electrons (Figure 1b).[11] The morphologies and size distributions of these LM microdroplets are shown in the scanning electron microscopy (SEM) image in Figure S3a (Supporting Information) and in (Section 4 of the Supporting Information), respectively.

The Ga-atom unpaired electrons reacted with the acrylamide-monomer π-bonds (Figure 1b),[11,12] initiating polymerization by covalent-bond formation between the EGaIn microdroplets and the acrylamide-monomer carbon atoms. Subsequently, the continuously generated free radicals caused cross linking with other monomers (Figure 1b). The LM-initialized polymerization converted the acrylamide aqueous solution to a polyacrylamide hydrogel containing hemicellulose microparticles. The hemicellulose microparticles form hydrogen bonds with the polyacrylamide chain (Figure 1c). As a result, the hydrogel contains two bonding systems with a covalent bond and a hydrogen bond (Figure 1d). The fabricated polyacrylamide-hemicellulose/EGaIn microdroplets hydrogel with carbon black was a viscoelastic composite and was subsequently used to 3D-print scaffolds and anode hosts for Zn-ion batteries (Figure 1e).

The hydrogel was initially identified using its FTIR spectrum (**Figure 2**a); an intensity reduction of the C=C vibration band at 1610 cm^{-1} confirmed the acrylamide-to-polyacrylamide conversion.[11] Subsequently, ^{1}H NMR was used to elucidate the polyacrylamide structure. As shown in the 1H NMR spectrum (Figure 2b), characteristic peaks at ≈1.48 ppm (methylene protons) and ≈2.04 ppm (methane protons) confirmed the existence of polyacrylamide;[11] a peak at ≈4.6 ppm corresponded to the $-CH_2-$ protons of polyacrylamide (Figure 2c).[12]

The time-dependent conversion of acrylamide during shear mixing was analyzed to elucidate the kinetics of acrylamide polymerization by the LM microdroplets (Figure 2d). With the progress of shear mixing from 0 to 40 min, acrylamide conversion increased from 0 to 100%, and the molecular weight of polyacrylamide increased from ≈70 to ≈577 486 g mol^{-1}. Moreover, the polydispersity, estimated by the ratio of the weight-average molecular weight and number-average molecular weight (M_w/M_n), of the resultant polyacrylamide is ≈2.84.

On stirring with a hemicellulose suspension, the polyacrylamide chains with EGaIn microdroplets interacted with the hemicellulose microparticles through hydrogen bonding between the hydroxyl groups and amine groups on hemicellulose and acrylamide (Figure 1c).[13] The molecular formula of hemicellulose and polyacrylamide, and the schematics of hydrogen-bond formation are shown in Figure S5 (Supporting Information). A strong absorption peak, attributed to the amino group, was observed at 3385 cm^{-1} in the FTIR spectra of acrylamide and polyacrylamide (Figure S6, Supporting Information).[14,15] The position of this peak shifted to 3410 cm^{-1} in the spectrum of the synthesized polyacrylamide-hemicellulose/EGaIn microdroplets polymer composite (Figure S6, Supporting Information), indicating that the polyacrylamide amino groups underwent hydrogen bonding with the hydroxyl groups of hemicellulose.[12,16] The morphology of hemicellulose and polyacrylamide are shown in Figure S3c (Supporting Information). After polymerization and chain growth, the polyacrylamide-hemicellulose/EGaIn microdroplets hydrogel exhibited a cross-linked 3D network (Figure S1f, Supporting Information) with uniformly distributed LM microdroplets (Figure S7, Supporting Information). The morphology and elemental distribution of the polyacrylamide-hemicellulose/EGaIn microdroplets hydrogel are described in (Sections 8, 9 of the Supporting Information).

During polymerization, the hemicellulose microparticles (Figure S3b, Supporting Information) significantly affected hydrogel homogenization. Hemicellulose microparticles, suspended inside the solution by stirring, prevented LM-microdroplet sinking during mixing. Additionally, a double covalent bond and hydrogen bonding is formed in the composite (Figure 1d). The hydrogen bonds are formed by the abundant hydroxyl groups on the hemicellulose surface and on the polyacrylamide chains (Figure S5, Supporting Information). Experiments confirmed the formation of a non-uniform polymer-composite dispersion in the absence of hemicellulose microparticles due to the sunken LM microdroplets to the bottom of the solution during shear mixing (Figure S10, Supporting Information).

The sunken LM microdroplets caused the bottom surface of the hydrogel to exhibit a grayish color (Figure S10, Supporting Information). SEM images show the different microstructures of the polyacrylamide hydrogel without hemicellulose microparticles (Figure S11, Supporting Information). The bottom part of the hydrogel contained a large number of LM microdroplets, densely dispersed inside the composite (Figure S11a–c, Supporting Information); one such LM microdroplet is circled in Figure S11c (Supporting Information). The middle part of the hydrogel contained comparatively fewer LM microdroplets (Figure S11d–f, Supporting Information).

Subsequently, dissolvable starch was used as an additive; it could not form LM-microdroplet suspensions by shear mixing (Figure S12, Supporting Information). A comparison of the hydrogels formed with hemicellulose and dissolvable starch confirmed that the hemicellulose microparticles ensure the formation of uniform LM-microdroplet suspension and hydrogel synthesis by shear mixing.

2.2. Fabrication of Printable Hydrogel Ink with Carbon Black

Carbon black (Super b) was added to the solution during polymerization to increase its electrical conductivity and adjust the rheological properties of the hydrogel (detailed information is provided in the Experimental Section). Rheological measurements of the composite hydrogel were conducted at ambient temperatures. As shown in Figure 2e, both of the LM-initialized polyacrylamide hydrogels formed with or without carbon black exhibited typical shear-thinning thixotropic fluid behavior, whereas the aqueous solutions of acrylamide and hemicellulose showed liquid characteristics with no shear-thinning behavior (Figure S13, Supporting Information). Unlike the hydrogel synthesized without carbon black, the hydrogel synthesized with carbon black exhibited a progressive reduction of viscosity from 5789.9 to

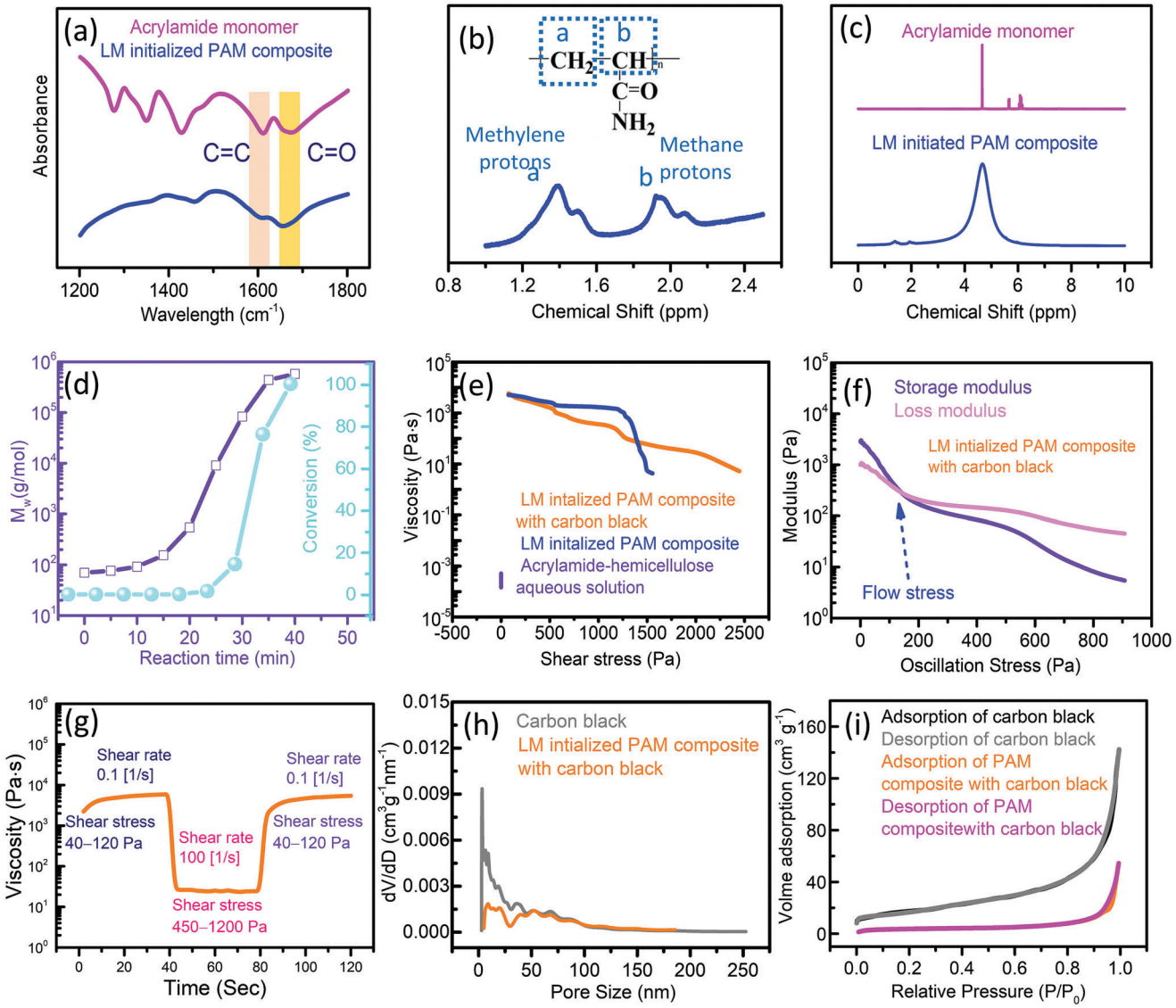

Figure 2. a) ATR FT-IR spectra of the acrylamide powder and LM initialized polyacrylamide(PAM)-hemicellulose composite. b) The ^{1}H NMR spectra (400 MHz, D_2O) illustrates that polyacrylamide was formed from a solution of liquid metal microdroplets, acrylamide, and hemicellulose. c) ^{1}H NMR spectra of acrylamide monomer, and liquid metal initialized polyacrylamide composite after shear mixing for 40 min. d) Dependence of molecular weight (g mol^{-1}) and ϵ-CL conversion (%) on the shear mixing time of the solution of EGaIn microdroplets, acrylamide, and hemicellulose. e) Viscosity changes of the polyacrylamide hydrogel composites and acrylamide-hemicellulose aqueous solution as a function of shear stress. f) Storage and loss modulus as a function of oscillation stress for the polyacrylamide hydrogel composite with carbon black. g) Ink viscosity progression over time with alternate low (0.1 s^{-1}) and high shear rates (100 s^{-1}) of the polyacrylamide hydrogel with carbon black presenting appropriate viscosity drop and recovery during and after ink extrusion through a nozzle. h) Pore size distribution and i) nitrogen adsorption and desorption of freeze-dried polyacrylamide hydrogel composites with and without carbon black.

5.2 Pa s on increasing the shear stress from 76.2 to 2446.7 Pa (Figure 2e).

The viscoelastic properties of the polyacrylamide-hemicellulose/EGaIn microdroplets hydrogel with and without carbon black were analyzed further by comparing their elastic/storage modulus (G′) and viscous/loss modulus (G″) values during oscillatory measurements (Figure 2f). The hydrogel with carbon black showed G′ and G″ values of 2973.6 and 1037.4 Pa, respectively, at a low shear stress (0.6 Pa), indicating an elastic solid-like behavior.[17] On increasing the shear stress to 141 Pa, the G′ value significantly reduced, becoming lower than the G″ value (Figure 2f), indicating a flow stress of ≈141 Pa. Similarly, the hydrogel without carbon black exhibited a drastic reduction of the G′ value on increasing the shear stress to 2474 Pa (Figure S14, Supporting Information). Oscillatory measurements indicated that both the hydrogels exhibited shear-thinning behavior with immense potential to be utilized as inks for extrusion-based 3D printing.[18]

To investigate the shear-thinning effect of the polyacrylamide-hemicellulose/EGaIn microdroplets hydrogel with carbon black

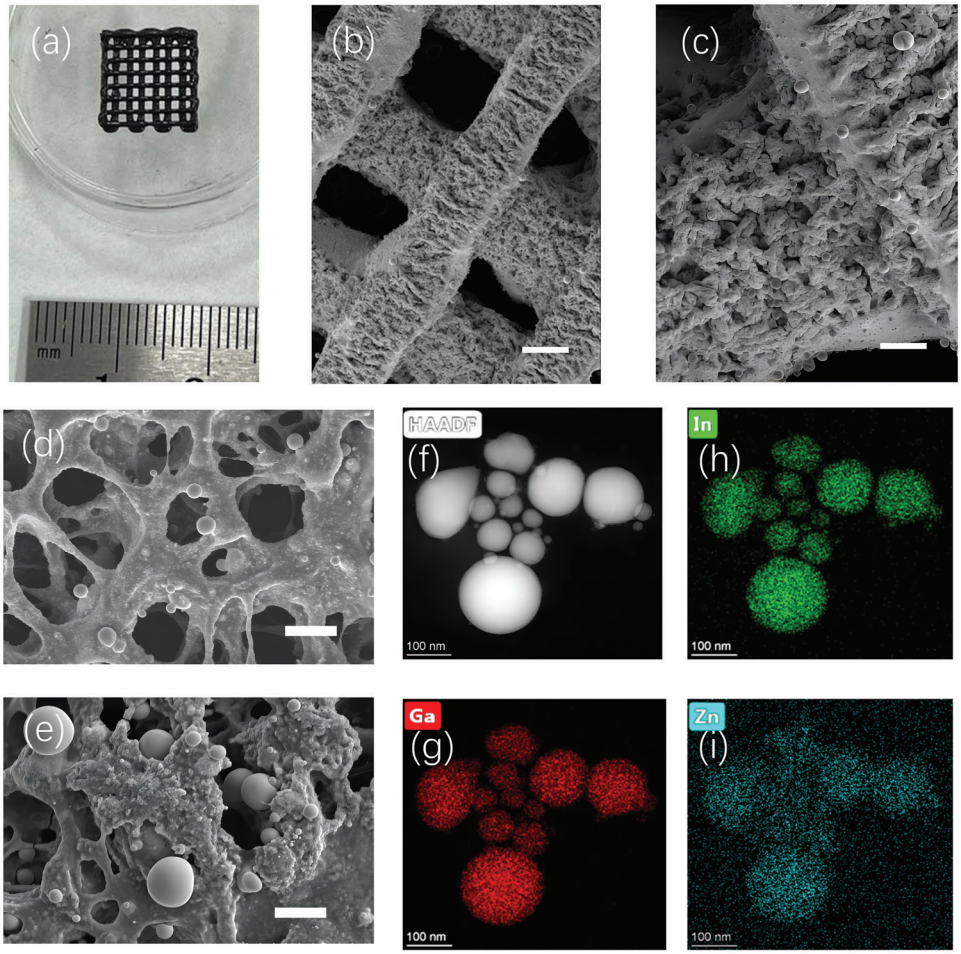

Figure 3. a) Digital photos of the 3D printed scaffold of polyacrylamide-hemicellulose/EGaIn microdroplets hydrogel with carbon black. SEM images of the scaffold with different scale bars of b) 350 µm, c) 90 µm. SEM images of d) freeze-dried polyacrylamide-hemicellulose/EGaIn microdroplets hydrogel with carbon black having a scale bar of 21 µm and e) the hydrogel after electrochemical deposition of Zn, having a scale bar of 17 µm. f) HAADF images and g–i) EELS elemental mapping results of the EGaIn nanoparticle with electrochemically deposited Zn.

during 3D printing, its extrusion behavior through a nozzle was analyzed using a thixotropic-behavior measurement at different shear rates and shear stresses (Figure 2g). On increasing the shear rate to 100 s^{-1} at a critical shear stress of ≈450 Pa, the viscosity of the hydrogel reduced drastically from 5800 to 24 Pa s (Figure 2g). The ink viscosity progression over time with alternate low (0.1 s^{-1}) and high (100 s^{-1}) shear rates exhibited the expected viscosity drop and recovery trends during and after ink extrusion through the nozzle. The combination of viscosity-recovery capability and shear-thinning behavior ensured the reliable 3D printing of complicated free-standing architectures.[19] Additionally, the rapid viscosity recovery of the hydrogel indicated that the polyacrylamide chains showed effective self-healing via hydrogen and covalent bonding.[20] This self-healing behavior has been discussed in detail in (Section 32 of the Supporting Information).

The LM-initialized polyacrylamide-hemicellulose/EGaIn microdroplets hydrogel with carbon black was used as an extrudable ink to print 3D architectures due to its suitable rheological properties (Video S1, Supporting Information). As shown in the 3D model (Figure S15, Supporting Information), the printed 3D architecture was a scaffold with a thickness of four layers (**Figure 3**a). Interestingly, unlike common hydrogel-based inks, the scaffold was a free-standing structure with span segments (Figure 3b) capable of supporting each other (Figure 3c), instead of being immersed together.[21] After freeze-drying, the LM microdroplets were distributed on the segment surface (Figure 3c). Due to the covalent bonding, even after the shearing effect during 3D printing, the LM microdroplets remained strongly connected within the polyacrylamide hydrogel composite. Subsequently, 3D architectures with different shapes were printed, as shown in Figure S16 (Supporting Information).

Apart from the scaffold, the hydrogel was used as an extrudable ink to print anode hosts. The hydrogel ink was printed on a titanium foil following the design shown in Figure S17a (Supporting Information); the printing process is shown in Video S2 (Supporting Information). The operation process of the software is shown in Figure S17a–c (Supporting Information). The printed hydrogel finally formed a square film with a side dimension of 8 mm (Figure S17d,e, Supporting Information). The program and Gcode used for 3D printing the electrode were illustrated in Section 18 of the Supporting Information. After printing and freeze drying, the printed film exhibited a porous microstructure

(Figure 3d) with a relatively uniform thickness of ≈150 µm thickness (Figures S19, S20a, Supporting Information) and ≈0.2 g weight. The morphology of the printed electrodes on Titanium foil is shown in Figure S19 (Supporting Information). According to measurements, 0.1 g of the porous composite with carbon black showed a specific surface area of 13.9 $m^2\ g^{-1}$ and a pore volume of 0.084 $cm^3\ g^{-1}$ (Figure 2h,i); this could be attributed to the presence of carbon black which exhibits a specific surface area of 56.01 $m^2\ g^{-1}$ and a pore volume of 0.22 $cm^3\ g^{-1}$ (Figure 2h,i). The specific area and pore volume of 0.1 g of the polyacrylamide-hemicellulose/EGaIn microdroplets composite without carbon black could not be estimated.

As indicated in Figure S17b,c (Supporting Information), the printed composite anode host featured porosity that allows the high utilization of zinc. Furthermore, it would inhibits the growth of zinc dendrite, endowing the batteries with high safety. In contrast, the doctor-bladed composite thin film possessed less porosity than the printed composite (Figure S20b,c, Supporting Information). The reason could be explained by that the movement of the blade break the interconnection of polyacrylamide within the composite, some part of the polyacrylamide was adhered to the edge of the blade. As the blade kept moving, some of the adhered polyacrylamides is coating on the film surface, which fills the pores on the film surface.

2.3. Fabrication and Tests of LM Initialized Polymer Composite with Zn

The freeze-dried polyacrylamide-hemicellulose/EGaIn microdroplets composite with carbon black exhibited a low surface resistivity of 41.0 µΩ $square^{-1}$ (Figure S21, Supporting Information) which is much lower than it of polyacrylamide-hemicellulose/EGaIn microdroplets composite without carbon black (Figure S22, Supporting Information). Due to the steady interconnection between carbon black and liquid metal microdroplets, the printed composite with deposited Zn (Figure S23, Supporting Information) has a similar surface resistivity of 4.48 mΩ $square^{-1}$ to it of pure Zn foil (5.03 mΩ $square^{-1}$) (Figure S24, Supporting Information).

After electrochemical deposition at 0.8 V for 2000 s in a $ZnSO_4$ electrolyte solution (1 M), the surface of the composite appeared to be slightly rough (Figure 3e) compared with the composite (Figure 3e). As indicated by the morphology and elemental distribution results (Figure 3e; Figure S25, Supporting Information), the composite exhibited a porous structure with a specific surface area of 11.9 $m^2\ g^{-1}$ and pore volume of 0.068 $cm^3\ g^{-1}$ (Figure S26, Supporting Information), with uniformly distributed Zn and negligible dendrite formation. This could be due to the polar amide-group-guided coordination adsorption of Zn^{2+} ions that produced relatively uniform nucleation sites for Zn deposition along the polyacrylamide chains.[22] Additionally, the high specific area of the 3D porous composite minimized the Zn-nuclei size, generating low stress in the network. In contrast, electrochemically deposited Zn on pure LM droplets generated abundant Zn dendrites on the LM (Figure S27, Supporting Information). A comparison of the Zn-deposited composites fabricated using different electrochemical deposition times indicated that the products formed after 2000 s deposition exhibited a stable microporous structure with uniform Zn deposition (Figure S28b, Supporting Information). The electrochemical deposition of Zn is discussed in (Sections 28–31 of the Supporting Information).

Subsequently, transmission electron microscopy (TEM) with element mapping was used to analyze Zn deposition on the LM microdroplets further. To fabricate small-size TEM samples (<200 nm) for the demand of TEM samples, the LM microdroplets with Zn were ultrasonicated, forming small-size nanodroplets. TEM images (Figure S32, Supporting Information) indicated the nanodroplet diameters to be in the range of 10–100 nm. High-angle annular dark-field (HAADF) images and electron energy loss spectroscopy (EELS) elemental mapping of the TEM data indicated a uniform distribution of Ga, In, and Zn (Figure 3f–i), with In distributed within the Ga matrix (Figure 3g,h). Subsequently, EELS confirmed the presence of Zn in the EGaIn nanodroplet (Figure 3i). The distribution of the various elements and mass ratios are provided in (Section 33 of the Supporting Information).

X-ray diffraction (XRD) was used to investigate the structure of the Zn-deposited LM microdroplets and compared it with that of pure Zn- and Ga-based liquid metals. The XRD spectrum of the Zn-deposited microdroplets exhibited the characteristic peaks of Zn and one broad peak at 30–40° due to the amorphous liquid-alloy phase, indicating the co-existence of the EGaIn liquid alloy and Zn.[23] All the relevant XRD patterns are shown in Figure S34 (Supporting Information).

2.4. Reversibility of Zn-Ion Plating/Stripping on the Composite

The high reversibility of Zn-ion plating/stripping ensures the long-term cycling stability of an anode in a 2 M $ZnSO_4$ electrolyte.[23] SEM and elemental mapping were used to confirm the reversibility of Zn-ion plating/stripping by analyzing the composite microstructure after 50 cycles of discharging/charging in symmetric cells at a current density of 0.5 mA cm^{-2}. SEM images (Figure S35a, Supporting Information) indicated that Zn-ion plating/stripping did not cause significant microstructure deformation or damage, and the LM microdroplets retained their spherical shape and remained interconnected within the polyacrylamide composite. The distribution and mass ratios of the different elements are provided in (Section 35 of the Supporting Information). The structure of the composite containing Zn was investigated and compared with that of pure Zn by X-ray photoelectron spectroscopy (Figure S36a, Supporting Information). Characteristic peaks confirmed the presence of Zn, Ga, In, and C in the composite, while the Zn $2p_{1/2}$ and Zn $2p_{3/2}$ peaks at 1044.46 and 1044.62 eV, respectively, confirmed the presence of ZnGaO (Figure S36b, Supporting Information).[24] Compared with pure Zn foil after charge and discharge, the Zn $2p_{3/2}$ peak position was shifted to a lower binding energy, indicating low Zn corrosion (Figure S36c, Supporting Information).[25,26]

The reversibility of the composite can be attributed to its double-bonding network. In this network, the covalent bonds formed by acrylamide polymerization could reconnect themselves, and the hydrogen bonds between the hemicellulose particles and polyacrylamide chains could dynamically break and reform, dissipating mechanical energy, during discharge/charging

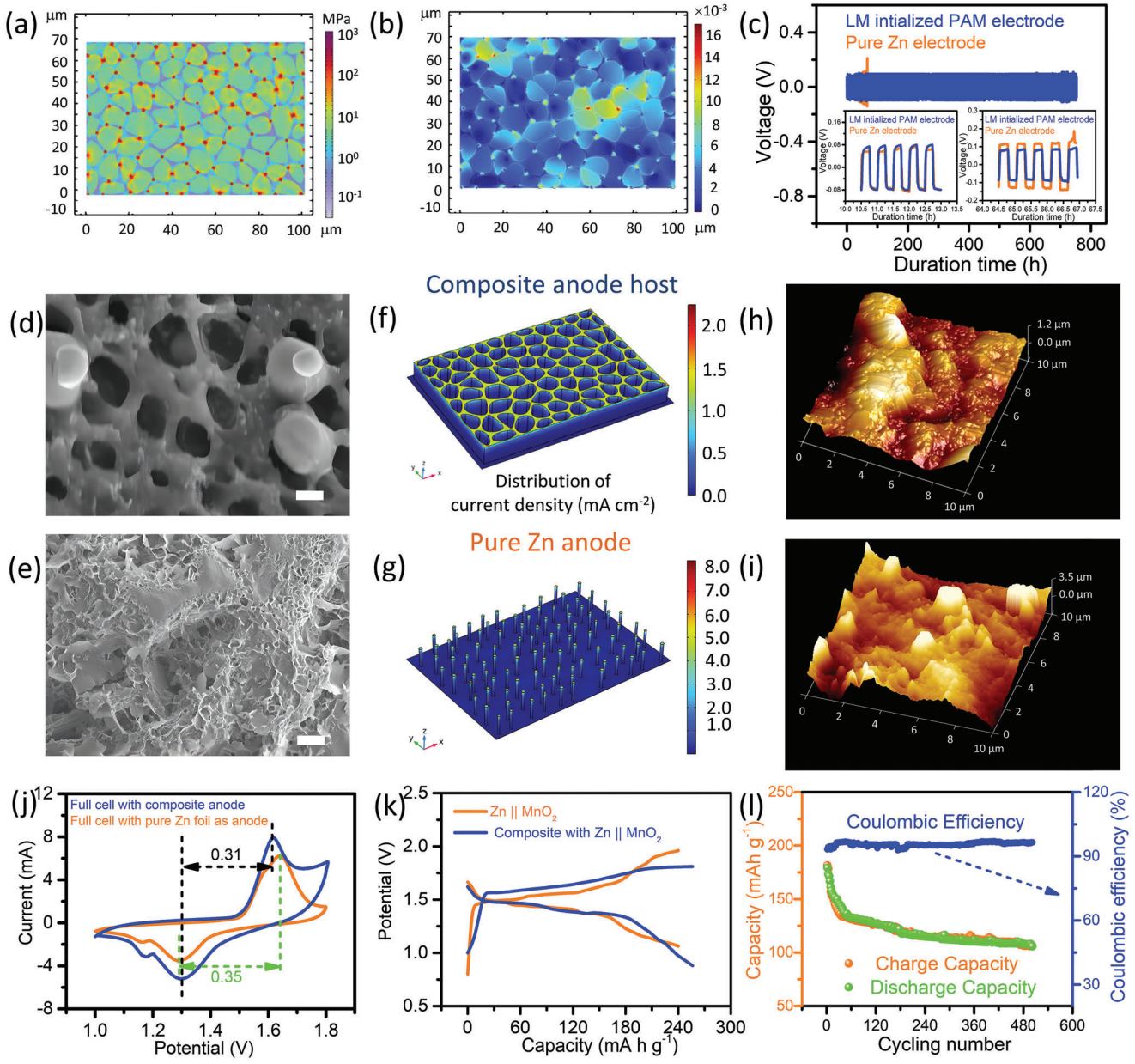

Figure 4. a) Simulated stress distribution and b) the deformation of the composite during Zn^{2+} plating/stripping. c) Galvanostatic cycling curves of the symmetric cells at a current density of 1.44 mA cm^{-2} with 0.36 mAh cm^{-2}. SEM images of d) the composite and e) pure Zn foil electrodes after 500 cycles of charging and discharging with scale bars of 2 µm. f) Simulated distributions of current density for the (f) composite and g) pure Zn foil electrodes. AFM images of the plated h) composite and i) pure Zn electrodes. j) CV curves of the full cells having polyacrylamide-hemicellulose/LM microdroplets composite or Zn foil as anode hosts at the scan rate of 10 mV s^{-1}. k) Galvanostatic charge/discharge profile of the full cells at the first cycle with the current density of 500 mA g^{-1}. l) Evaluation of the long-term cycling stability of the composite–MnO_2 full cell at 500 mA g^{-1}.

cycling.[27] The experimental results and mechanism of the self-healing capability of the polymer composite are provided in (Sections 37–40 of the Supporting Information). The polyacrylamide-hemicellulose/EGaIn microdroplets composite could steadily flow in a 2 M $ZnSO_4$ electrolyte solution for more than 3 months without significant deformation (Figure S41, Supporting Information).

A finite element calculation using the COMSOL Multiphysics 6.0 software was used to investigate the stress distribution of the composite during continuous Zn^{2+} plating/stripping (detailed information is provided in the Experimental Section). As shown in **Figure 4**a and Figure S42a–c (Supporting Information), the elastic polyacrylamide network generated a low (1–10 MPa) and relatively uniform stress distribution. In the composite network, the relatively rigid hemicellulose dissipated the inner stress, while the elastic polyacrylamide network dispersed the residual stress to alleviate the composite-surface stress (where the Zn layer was deposited).[28] The LM microdroplets, connected

within the network through covalent bonds, could deform to withstand stress due to their fluidity and flexibility. Thus, the LM-initialized porous polyacrylamide network could progressively disperse inner stresses during Zn^{2+} plating/stripping, causing very low deformation (Figure 4b; Figure S42d–f, Supporting Information).[29] Consequently, it could inhibit LM-microdroplet delamination, maintaining its structural integrity.

Symmetric batteries with the composite showed higher cycling stability than those utilizing pure Zn foil (Figure 4c). The composite exhibited a long lifetime of over 700 h (up to 1500 cycles) with a low voltage hysteresis (178 mV at a current density of 1.44 mA cm^{-2}). In contrast, the pristine Zn anode exhibits a lifetime of only 67 h (up to 134 cycles) with a high voltage hysteresis of 274 mV under the same conditions. The cycling behavior of the composite in a symmetric battery is compared with previous work in Section 43 of the Supporting Information.[30–35] The composite also exhibited a longer lifetime of 1060 cycles with a low voltage hysteresis (114 mV at a current density of 0.72 mA cm^{-2}) than the pristine Zn anode (Figure S44, Supporting Information). Thus, the composite exhibited a longer lifetime and lower interface impedance.[23] The microstructures of the composite and pure Zn after 500 cycles at a current density of 0.72 mA cm^{-2} are shown in Figure 4d,e. The polyacrylamide chains with Zn still maintain the porous microstructure (Figure 4d) and the LM microdroplets were still bonded with the polyacrylamide chains (Figure S45, Supporting Information). The morphology and element mapping results of the composite after the cyclic Zn plating/stripping in symmetric batteries were indicated in Sections 45 and 46 of the Supporting Information. In contrast, the Zn-foil surface exhibited numerous Zn dendrites (Figure 4e) that caused rapid polarization and high-voltage hysteresis.[36]

Moreover, to further understand the dependence of Zn^{2+} conductivity of the composite with deposited Zn, electrochemical impedance spectroscopy (EIS) was performed before and after 100 cycles. The EIS measurement result in Figure S47 (Supporting Information) indicates the charge-transfer resistance (R_{ct}) of symmetric cells with the composite having deposited Zn and pure Zn foils. The charge transfer resistance of the symmetric cell with composite having deposited Zn (173 Ω) is much smaller than the case of pure Zn (539 Ω) after 100 cycles. It indicates the fast charge transfer and Zn plating/stripping kinetics of the composite with deposited Zn and lower polarization. The result for the fast charge transfer and lower polarization could be explained by that the composite with deposited Zn has reduced interfacial resistance than pure Zn and the liquid metal microdroplets in the composite could prove a strong affiliation with the absorbed Zn^{2+}. As a result, the composite with carbon black and deposited Zn has the capability to ameliorate the electrodeposition process of zinc with lower polarization and interface resistance at the Zn plating process.[22]

To analyze the effect of the composite anode on the Zn plating behavior further, the local current density, electric field distribution, and ion distribution of Zn^{2+} at the interface between the composite and electrolyte were simulated using the COMSOL Multiphysics software 6.0. A 3D model of the composite was constructed using SEM images to simulate the composite microstructure (Figure S48, Supporting Information). As shown in Figure 4f, the composite exhibited a continuous conductive porous structure with an ability to dissipate the current density. Current-density dissipation (Figure S49a, Supporting Information) prevented charge accumulation, generating a relatively uniform electric-field distribution on the composite electrode surface (Figure S49b, Supporting Information). Consequently, the Zn^{2+} flux at the electrode surface was relatively uniform, with negligible high-concentration spots (Figure S49c, Supporting Information). In contrast, the distribution of electric field on the pure Zn foil surface was inhomogeneous (Figure 4g; Figure S50a, Supporting Information), with higher electric fields near the isolated Zn-nuclei sites compared with other regions (Figure S50b, Supporting Information). The simulation results are provided in (Sections 49, 50 of the Supporting Information).

To confirm the relatively uniform deposition of Zn on the composite and verify the simulation result, the cross-sectional interfacial morphologies of pure Zn and the composite were recorded by in situ operando optical microscopy. Pure Zn foil exhibited a bumpy surface consisting of chaotic clusters and dendrites after Zn plating at 10 mA cm^{-2} for 3000 s (Figure S51a, Supporting Information). In contrast, no sharp dendrites were observed on the composite surface using various Zn plating times (Figure S51b, Supporting Information). Additionally, the specimen surfaces were analyzed by Atomic force microscopy (AFM) to verify the simulation results. Compared with the non-plated composite surface (Figure S52a, Supporting Information), the plated composite surface exhibited a slight modification (Figure 4h), with a height difference of ≈0.1 μm (Figure S52b, Supporting Information), confirming a relatively uniform and confined Zn deposition during the reaction. In contrast, significant morphology modification was observed on the Zn foil; tips were observed on the Zn-foil surface after deposition (Figure S53, Supporting Information). The AFM image (Figure 4i) indicated the Zn tips at the image. The tip height of the plated Zn foil (up to 3.5 μm) was higher than that of the plated composite (Figure 4h). Compared with the initial Zn foil, the plated Zn foil exhibited a height difference of up to ≈3.0 μm (Figure S54, Supporting Information).

2.5. Performance of the Zn-Ion Batteries

After investigating the internal-structure modification on discharging/charging, the practicability of this polyacrylamide-hemicellulose/EGaIn microdroplets hydrogel was confirmed. A full-cell (Figure S55, Supporting Information) measurement was conducted by pairing the composite with a typical MnO_2 cathode in an electrolyte containing $ZnSO_4$ (2 M) and $MnSO_4$ (0.1 M). MnO_2 was electrochemically deposited on carbon cloth and used as the cathode electrode (Figure S56, Supporting Information). The CV curve of this cell (Figure 4j) showed redox peaks similar to those exhibited by full cells, with a reduced peak polarization, using pure Zn anodes, indicating enhanced Zn^{2+} diffusion kinetics at the electrode.[23] Except for the first cycling, similar intensities of redox peaks were observed in subsequent cycles; this indicated reversible Zn^{2+} plating/stripping (Figure S57a, Supporting Information).[37]

The two reduction peaks at 1.15 and 1.32 V (Figure 4j) could be attributed to Zn^{2+} insertion in MnO_2 and the reduction of manganese, corresponding to the discharging plateaus at 1.27 and 1.36 V in the galvanostatic charge/discharge profiles

(Figure S57b, Supporting Information). The oxidation peak at 1.65 V (Figure 4j) could be attributed to Zn^{2+} stripping and the consequent recovery of the manganese valence state, corresponding to the charging plateaus at 1.46 V (Figure S57b, Supporting Information).[38,39] Furthermore, the battery with the composite exhibited a lower attenuation in capacity in the galvanostatic charge/discharge profiles than that using pure Zn (Figure 4k; Figure S57c, Supporting Information). The rate performance of the full cell was evaluated in the range of 1 C–10 C; it exhibited capacities in the range of 238.5–118.8 mAh g^{-1} (Figure S57d, Supporting Information) which is better than those of the full cell with pure Zn anode (Figure S57e, Supporting Information).

Electrochemical impedance spectroscopy measurement result indicated effective electrochemical processes and rapid ion transfer by the composite. The Nyquist plots were fitted by an equivalent circuit, as shown in the inset of Figure S58a (Supporting Information). The first arc with a small diameter remained unchanged during cycling, indicating a stable electrochemical performance of the interfacial impedance resistance (R_f) (Figure S58a, Supporting Information). The lower interfacial impedance (R_f) and charge-transfer resistance (R_{ct}) compared to that of pure Zn electrodes (Figure S58b, Supporting Information) indicated rapid Zn-ion transport at the electrode/electrolyte interface (Table S1, Supporting Information).[23]

The cycling performance of the cell is shown in Figure 4l. A specific capacity of ≈210 mAh g^{-1} was maintained at 500 mA g^{-1} after 1000 cycles. The full cell of the composite anode host is able to undertake cyclic Zn plating/striping at a current density of 1000 mA g^{-1} (Figure S59b, Supporting Information). The full cell with the composite exhibited a more stable cycling performance which is illustrated in (Section 60 of the Supporting Information) than that using pure Zn foil at a current density of 1000 and 500 mA g^{-1}. The behavior of the full cell with composite anode host is also compared with previous works in Section 61 of the Supporting Information.[30,33,40–42] The morphology and element mapping results of the composite after 500 cyclic Zn plating/stripping are presented in (Section 62 of the Supporting Information).

The reason for the longer stability of the composite could be attributed to its porous structure and the effect of liquid metal microdroplets. First, the porous structure can provide selective nucleation sites for Zn deposition[22] (Figure 4f; Figure S50, Supporting Information) and possesses self-healing capacity (Figure S37, Supporting Information) that progressively dispersed inner stresses during charge/discharge (Figure 4a; Figure S42, Supporting Information).[28] As shown in Figure S62 (Supporting Information), the bonded polymer prevented LM-microdroplet delamination during charging and discharging. The porous structure of the composite host could limit dendrite growth (Figure S63a, Supporting Information) to a greater extent than pure Zn foil (Figure S63b, Supporting Information), and the self-healing capability of the hydrogel enabled structural deformations without significant cracks.[43]

Second, the addition of EGaIn in the composite could affect the Zn ion transfer and improve the stability. As depicted in Figure S64a,b (Supporting Information), after 100 cycles at a current density of 1 mA cm^{-2}, the hysteresis voltage in the galvanostatic voltage profiles of half-cell having composite anode host is 77 mV which is lower than that of the pure Zn (≈148 mV). The Tafel curve (Figure S64c, Supporting Information) illustrates the increase in the self-corrosion potential of the composite from −1.03 to −1.01 V, which means the composite has the capability to resist the corrosion of the $ZnSO_4$ aqueous electrolyte at a current density of 1 mV s^{-1}. According to the result, the composite anode host would exhibit decreased polarization than pure Zn, corresponding to easier plating/stripping of the Zn ion.

These results could be further explained by the process in Figure S65 (Supporting Information). The Zn on the composite is connected by the EGaIn microdroplets, which have higher redox potentials than pure Zn (−0.338 V vs the standard hydrogen electrode of indium and −1.0V vs the standard hydrogen electrode of Gallium oxide).[44,45] As a result, due to the existence of polarization caused by the higher redox potentials between EGaIn and Zn, the electrons from external circuits are more inclined to accumulate on the EGaIn, resulting in the accumulation of negative electrons on EGaIn.[46] Consequently, during the charging process, the Zn^{2+} in the aqueous electrolyte tends to be adsorbed on EGaIn where the Zn ion obtains electrons and then is reduced to Zn. During the discharging process, due to the accumulated positive charges on the surface, the Zn which are adjacent to EGaIn tends to lose electrons and convert to more stable Zn^{2+} to dissolve into the electrolyte. Therefore, the incorporation of EGaIn microdroplets could be conducive to the plating/stripping of Zn^{2+} in the composite.

In brief, the stability of the composite can be attributed to the porosity of the composite hindering the growth of Zn dendrite;[47] the LM microdroplets having high affinity to Zn to ensure the stability of the composite;[22,46] and the intertwining interaction between polyacrylamide and hemicellulose effectively suppressing the volume deformation of the composite during cyclic charge/discharge processes.[26] Additionally, the electrochemical performance of the composite in half-cells was investigated and the results are provided in (Section 65 of the Supporting Information).

3. Conclusion

In this study, the shear mixing of EGaIn initiated the free-radical polymerization of acrylamide, producing a multifunctional polyacrylamide hydrogel ink by a facile procedure. The polyacrylamide hydrogel showed a good rheological performance and self-healing capability; thus, it was utilized as an extrudable ink for 3D-printing free-standing architectures and an anode host for Zn-ion batteries. The self-healing property, high electrical conductivity, and porous structure of the hydrogel composite with deposited Zn enabled Zn-ion cyclic plating/stripping without structural deformation, LM-microdroplet loss, and Zn dendrite growth. Therefore, free-radical polymerization by the shear mixing of EGaIn would be used as an effective strategy to fabricate multifunctional liquid metal-based polymer composites for energy storage devices, flexible electronics, and smart materials.

Supporting Information

Supporting Information is available from the Wiley Online Library or from the author.

Acknowledgements

This work was supported by the State Key Laboratory of Pulp and Paper Engineering (Grant No. 2022PY02), National Natural Science Foundation of China (52003083, 31971614 and 32071714), National Program for Support of Top-notch Young Professionals (x2qsA4210090), Guangdong Basic and Applied Basic Research Foundation (Grant No. 2023B1515040013 2022A1515011801, 2021A1515110205), Key Project of Guangzhou Scientific Research Project (SL2022B03J01256) and Fundamental Research Funds for the Central Universities (Grant No. 2022ZYGXZR019 and 2019PY13).

Conflict of Interest

The authors declare no conflict of interest.

Data Availability Statement

The data that support the findings of this study are available on request from the corresponding author. The data are not publicly available due to privacy or ethical restrictions.

Keywords

3D printing, anode hosts, free-radical polymerization, liquid metal microdroplets, Zn-ion batteries

Received: January 4, 2023
Revised: March 15, 2023
Published online: April 28, 2023

[1] R. R. Kohlmeyer, A. J. Blake, J. O. Hardin, E. A. Carmona, J. Carpena-Núñez, B. Maruyama, J. D. Berrigan, H. Huang, M. F. Durstock, *J. Mater. Chem. A* **2016**, *4*, 16856.
[2] L. Li, W. Liu, H. Dong, Q. Gui, Z. Hu, Y. Li, J. Liu, *Adv. Mater.* **2021**, *33*, 2004959.
[3] J. Gu, Y. Tao, H. Chen, Z. Cao, Y. Zhang, Z. Du, Y. Cui, S. Yang, *Adv. Energy Mater.* **2022**, *12*, 2200115.
[4] T. Chu, S. Park, K. Fu, *Carbon Energy* **2021**, *3*, 424.
[5] a) W. Xu, X. Liao, W. Xu, C. Sun, K. Zhao, Y. Zhao, C. Hu, *Nano Energy* **2021**, *88*, 106237; b) H. Jiao, S. Jiao, S. Li, W.-L. Song, H. Chen, J. Tu, M. Wang, D. Tian, D. Fang, *Chem. Eng. J.* **2020**, *391*, 123594.
[6] Y. Ding, X. Guo, G. Yu, *ACS Cent. Sci.* **2020**, *6*, 1355.
[7] Y. Fan, T. Tao, Y. Gao, C. Deng, B. Yu, Y. Chen, S. Lu, S. Huang, *Adv. Mater.* **2020**, *32*, 2004798.
[8] J. Yan, M. H. Malakooti, Z. Lu, Z. Wang, N. Kazem, C. Pan, M. R. Bockstaller, C. Majidi, K. Matyjaszewski, *Nat. Nanotechnol.* **2019**, *14*, 684.
[9] S. Y. Zheng, Y. Shen, F. Zhu, J. Yin, J. Qian, J. Fu, Z. L. Wu, Q. Zheng, *Adv. Funct. Mater.* **2018**, *28*, 1803366.
[10] J. Ma, Y. Lin, Y.-W. Kim, Y. Ko, J. Kim, K. H. Oh, J.-Y. Sun, C. B. Gorman, M. A. Voinov, A. I. Smirnov, *ACS Macro Lett.* **2019**, *8*, 1522.
[11] X. Li, M. Li, Q. Shou, L. Zhou, A. Ge, D. Pei, C. Li, *Adv. Mater.* **2020**, *32*, 2003553.
[12] Q. Fu, S. Hao, L. Meng, F. Xu, J. Yang, *ACS Nano* **2021**, *15*, 18469.
[13] E. Patyukova, T. Rottreau, R. Evans, P. D. Topham, M. J. Greenall, *Macromolecules* **2018**, *51*, 7032.
[14] X. Liu, S. Luan, W. Li, *Int. J. Biol. Macromol.* **2019**, *132*, 954;
[15] X. Liu, M. Chang, H. Zhang, J. Ren, *Colloids Surf.* **2022**, *647*, 129024.
[16] Y. Zhang, G. Shi, J. Qin, S. E. Lowe, S. Zhang, H. Zhao, Y. L. Zhong, *ACS Appl. Electron. Mater.* **2019**, *1*, 1718.
[17] W. Zhang, R. Wang, F. Luo, P. Wang, Z. Lin, *Chin. Chem. Lett.* **2020**, *31*, 589.
[18] S. Uman, A. Dhand, J. A. Burdick, *J. Polym. Sci.* **2020**, *137*, 48668.
[19] L. Li, Q. Lin, M. Tang, A. J. Duncan, C. Ke, *Chemistry* **2019**, *25*, 10768.
[20] A. E. Jakus, E. B. Secor, A. L. Rutz, S. W. Jordan, M. C. Hersam, R. N. Shah, *ACS Nano* **2015**, *9*, 4636.
[21] J. Yang, B. Yin, Y. Sun, H. Pan, W. Sun, B. Jia, S. Zhang, T. Ma, *Nano-Micro. Lett.* **2022**, *14*, 42.
[22] C. Liu, Z. Luo, W. Deng, W. Wei, L. Chen, A. Pan, J. Ma, C. Wang, L. Zhu, L. Xie, *ACS Energy Lett.* **2021**, *6*, 675.
[23] H. H. Kim, D. O. Kumi, K. Kim, D. Park, Y. Yi, S. H. Cho, C. Park, O. Ntwaeaborwa, W. K. Choi, *RSC Adv.* **2019**, *9*, 32066.
[24] D. Lee, H. I. Kim, W. Y. Kim, S. K. Cho, K. Baek, K. Jeong, D. B. Ahn, S. Park, S. J. Kang, S. Y. Lee, *Adv. Funct. Mater.* **2021**, *31*, 2103850.
[25] V. T. Tran, M. T. I. Mredha, S. K. Pathak, H. Yoon, J. Cui, I. Jeon, *ACS Appl. Mater. Interfaces* **2019**, *11*, 24598.
[26] L. Ma, S. Chen, D. Wang, Q. Yang, F. Mo, G. Liang, N. Li, H. Zhang, J. A. Zapien, C. Zhi, *Adv. Energy Mater.* **2019**, *9*, 1803046.
[27] X. Jiao, J. Yin, X. Xu, J. Wang, Y. Liu, S. Xiong, Q. Zhang, J. Song, *Adv. Funct. Mater.* **2021**, *31*, 2005699.
[28] Q. Yang, Q. Li, Z. Liu, D. Wang, Y. Guo, X. Li, Y. Tang, H. Li, B. Dong, C. Zhi, *Adv. Mater.* **2020**, *32*, 2001854.
[29] J. Han, H. Euchner, M. Kuenzel, S. M. Hosseini, A. Gross, A. Varzi, S. Passerini, *ACS Energy Lett.* **2021**, *6*, 3063.
[30] C. Deng, X. Xie, J. Han, Y. Tang, J. Gao, C. Liu, X. Shi, J. Zhou, S. Liang, *Adv. Funct. Mater.* **2020**, *30*, 2000599.
[31] B. Raza, Y. Zhang, M. Xu, J. Yang, Y. NuLi, J. Wang, *Chem. Eng. J.* **2022**, *447*, 137496.
[32] C. Liu, Z. Li, X. Zhang, W. Xu, W. Chen, K. Zhao, Y. Wang, S. Hong, Q. Wu, M. C. Li, *Adv. Sci.* **2022**, *9*, 2202380.
[33] F. Wu, Y. Chen, Y. Chen, R. Yin, Y. Feng, D. Zheng, X. Xu, W. Shi, W. Liu, X. Cao, *Small* **2022**, *18*, 2202363.
[34] H. Qin, W. Kuang, N. Hu, X. Zhong, D. Huang, F. Shen, Z. Wei, Y. Huang, J. Xu, H. He, *Adv. Funct. Mater.* **2022**, *32*, 2206695.
[35] Z. Zhang, X. Yang, P. Li, Y. Wang, X. Zhao, J. Safaei, H. Tian, D. Zhou, B. Li, F. Kang, *Adv. Mater.* **2022**, *34*, 2206970.
[36] B. W. Olbasa, F. W. Fenta, S.-F. Chiu, M.-C. Tsai, C.-J. Huang, B. A. Jote, T. T. Beyene, Y.-F. Liao, C.-H. Wang, W.-N. Su, *ACS Appl. Energy Mater.* **2020**, *3*, 4499.
[37] a) J. Wang, J. G. Wang, H. Liu, Z. You, Z. Li, F. Kang, B. Wei, *Adv. Funct. Mater.* **2021**, *31*, 2007397; b) X. Liu, J. Yi, K. Wu, Y. Jiang, Y. Liu, B. Zhao, W. Li, J. Zhang, *Nanotechnology* **2020**, *31*, 122001.
[38] J. Zhou, M. Xie, F. Wu, Y. Mei, Y. Hao, L. Li, R. Chen, *Adv. Mater.* **2022**, *34*, 2106897;
[39] B. Zhou, C. Zuo, Z. Xiao, X. Zhou, D. He, X. Xie, Z. Xue, *Chemistry* **2018**, *24*, 19200.
[40] T. C. Li, Y. Lim, X. L. Li, S. Luo, C. Lin, D. Fang, S. Xia, Y. Wang, H. Y. Yang, *Adv. Energy Mater.* **2022**, *12*, 2103231.
[41] F. Wu, X. Gao, X. Xu, Y. Jiang, X. Gao, R. Yin, W. Shi, W. Liu, G. Lu, X. Cao, *ChemSusChem* **2020**, *13*, 1537.
[42] Y. Zhang, Y. Liu, Z. Liu, X. Wu, Y. Wen, H. Chen, X. Ni, G. Liu, J. Huang, S. Peng, *J. Energy Chem.* **2022**, *64*, 23.
[43] Y. Jiang, D. Ba, Y. Li, J. Liu, *Adv. Sci.* **2020**, *7*, 1902795.
[44] C. Kim, C. R. Lee, J. Heo, S. M. Choi, D.-H. Lim, J. Cho, S. Chung, J. R. Kim, *Bioresour. Technol.* **2018**, *258*, 203;
[45] J. H. So, H. J. Koo, M. D. Dickey, O. D. Velev, *Adv. Funct. Mater.* **2012**, *22*, 625.
[46] P. Xiao, H. Li, J. Fu, C. Zeng, Y. Zhao, T. Zhai, H. Li, *Energy Environ. Sci.* **2022**, *15*, 1638.
[47] Y. Son, S. Sim, H. Ma, M. Choi, Y. Son, N. Park, J. Cho, M. Park, *Adv. Mater.* **2018**, *30*, 1705430.